Robotica (2024), **42**, pp. 3934–3956
doi:10.1017/S0263574724001735

CAMBRIDGE UNIVERSITY PRESS

RESEARCH ARTICLE

Shape deformation analysis and dynamic modeling of a switchable rigid-continuum robot

Yixiong Du[1,2], Shuo Zhang[3], Zhongkai Zhang[2] and Hao Wang[3]

[1]Department of Biomedical Engineering, City University of Hong Kong, Hong Kong SAR, China
[2]Centre for Artificial Intelligence and Robotics (CAIR), Hong Kong Institute of Science & Innovation, Chinese Academy of Sciences, Hong Kong SAR, China
[3]Interdisciplinary Science Hub(ISH), Hypercycle Venture, Beijing, China
Corresponding author: Hao Wang; Email: whtxtian@gmail.com

Received: 18 March 2024; **Revised:** 2 September 2024; **Accepted:** 17 September 2024;
First published online: 7 November 2024

Keywords: rigid-continuum robots; variable curvature; equivalent concept; deformable behavior; dynamics modeling

Abstract

Continuum robots offer unique advantages in performing tasks within extremely confined environments due to their exceptional dexterity and adaptability. However, their soft materials and elastic structures inherently introduce nonlinearity and shape instability, especially when the robot encounters external contact forces. To address these challenges, this paper presents a comprehensive model and experimental study to estimate the shape deformation of a switchable rigid-continuum robot (SRC-Bot). The kinematic analysis is first conducted to specify the degrees of freedom (DoF) and basic motions of SRC-Bot, including motion of bending, rotating, and elongating. This analysis assumes that the curvature varies along the central axis and maps the relationship between joint space and driven space. Subsequently, an equivalence concept is proposed to unify the stiffness addressing each DoF, which is then utilized in the establishment of the dynamic model. According to the mechanical structural design, the deformed posture of SRC-Bot is discretized into five segments, corresponding to the distribution of the guiders. The dynamics model is then derived using Newton's second law and Euler's method to simulate the deformation under gravity, friction, and external forces. Additionally, the stiffness in three directions is quantified through an identification process to complete the theoretical model. Furthermore, a series of experiments are conducted and compared with simulated results to validate the response and deformed behavior of SRC-Bot. The comparative results demonstrate that the proposed model-based simulation accurately captures the deformable characteristics of the robot, encompassing both static deformed postures and dynamic time-domain responses induced by external and actuation forces.

1. Introduction

Continuum robots seek superior motion performance with unique flexibility, adaptability, and dexterity by taking advantage of soft material and smart compliant mechanisms [1, 2]. Increasing research efforts are being devoted to the mechanical design, precise modeling approach, and efficient control strategies to promote the deployment of continuum robots in diverse applications, particularly in extreme environments characterized by confined, narrow and harmless space [3, 4], for example, surgery in the human body [5, 6], and grasping soft objects [7].

An accurate model provides a significant way to comprehend the motion principle and behavior of continuum robots. Kinematics is commonly employed for analyzing shape deformation, disregarding the force [8], with the prevailing approach assuming constant curvature of continuum robots [9]. Furthermore, kinematic characteristics, for example, displacement, velocity, and acceleration, can be derived for mapping specific motion parameters through analytical geometry [10]. However, pure

kinematics, assuming a single constant curvature, fails to accurately capture the deformable feature of the continuum robot, especially in the presence of gravity and external loads.

Therefore, mechanics plays a crucial role in the behavior analysis of a dynamic continuum robot by incorporating various force factors in addition to kinematics. Hence, an effective dynamic modeling approach essentially influences the precise analysis and control of continuum robots [11, 12], whereas the nonlinearity and instability arising from the soft materials and flexible structures challenge the improvement of modeling [13].

Thus, various approaches were presented based on different discretization methods and mechanics theorem in order to acquire an accurate and efficient model that be deployed into simulating and controlling the deformation of continuum robots [14, 15]. From the discretization perspective, the piecewise constant curvature assumption is widely used in the basic deformation analysis of continuum robots [16–18]. It characterizes the shape of the robot as a series of mutually tangent circular arcs and can effectively simplify the modeling, which has been successfully applied to the workspace analysis and trajectory-tracking [19]. However, challenges become more obvious when the global shape of continuum robots needs to be accurately specified and controlled. To address this, the Bezier curve is applied to achieve the shape reconstruction for wire-driven continuum robots [20]. Similarly, an approach based on the piecewise cubic Bézier curve has been proposed for the shape control of a cable-driven soft manipulator by using a visual servoing technique [21].

From the perspective of the analysis method, low-fidelity lumped parameters and high-fidelity distributed parameters are commonly deployed in model establishment [22]. Low-fidelity lumped parameter models assume that each actuated segment of the robot is capable of being characterized by a single circular arc, and the high-fidelity distributed model represents the continuum robot with a spatial parameterized curve or a 3-D volume. A typical lumped method that uses the Euler–Lagrange method to formulate a Lagrangian in terms of the kinetic energy contributed by robotic motion and potential energy extracted from the gravity effect and elastic potential [23, 24]. The distributed models previously studied are known for their high fidelity, as they enable the continuum robots to adopt an arbitrary shape in response to applied loading. For example, Cosserat theory is explored to acquire a precise dynamics model, considering the external load [25, 26]. To address the difficulties of computation, a real-time numerical framework is proposed for solving the Cosserat-based dynamic models [27]. In addition, Hamilton's principle could be employed to derive a discrete model of continuum robots using a helicoidal shape function to achieve higher computational efficiency [28]. Moreover, a high-fidelity dynamic model is presented using the principle of virtual power considering the cable constraint and friction effect [29].

The contributions of this work are summarized as follows:

1. A novel design of a continuum robot capable of switching its configuration to achieve various levels of stiffness.
2. A modeling approach with variable curvature-torsion-length for a switchable rigid-continuum robot, specifying the deformation response and behavior under different actuations and external forces. The proposed model considers external forces acting not only on the robot's tip but also on its body, allowing for a comprehensive analysis of the robot's deformable behavior.
3. A dynamics model formulated using Newton's second law and Euler's principle, incorporating the influences of gravity, friction, and external forces. This model integrates an equivalent concept to determine stiffness parameters.
4. Validation of the model through both numerical simulations and experiments, with results effectively demonstrating the model's ability to reflect the dynamic shape characteristics of the proposed robot.

The content is structured as follows: Section 2 introduces the concept and structural design of SRC-Bot. In Section 3, a discretization method is proposed for establishing the kinematics with the

https://doi.org/10.1017/S0263574724001735 Published online by Cambridge University Press

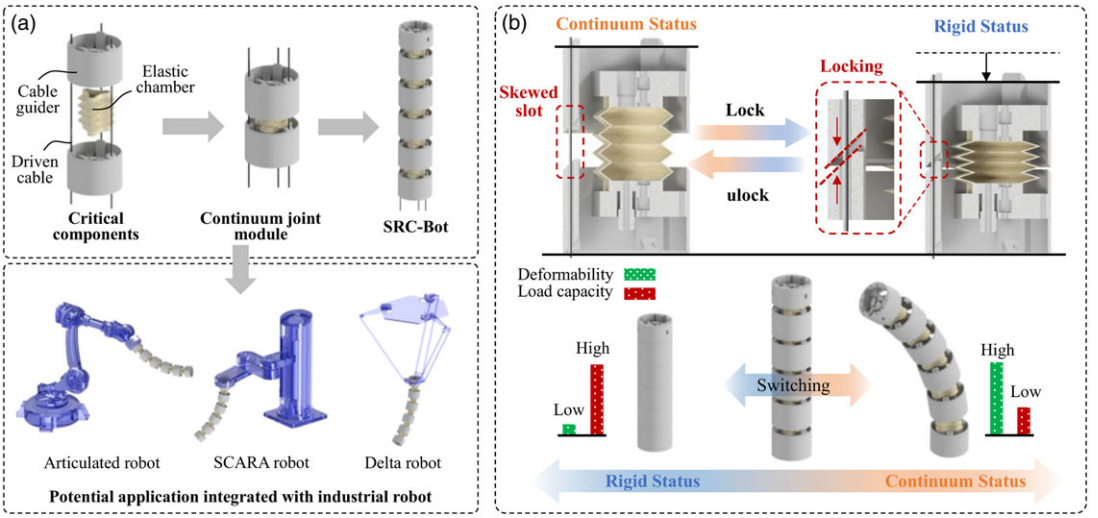

Figure 1. *Schematic diagram of structure design and brief introduction of SRC-Bot: (a) Concept, structure, and potential scenario; (b) switchable principle of SRC-Bot.*

assumption of constant and variable curvature. A dynamics model with an equivalent stiffness concept is established in Section 4 by considering the gravity, friction, and external force based on the discretization approach. Furthermore, the proposed dynamics model is integrated into SIMULINK for simulating various motions in Section 5. Consequently, several experiments were conducted to identify the stiffness and validate the deformation response and behavior by comparing them with the simulation results in Section 6. Finally, the conclusion and the future work are discussed in Section 7.

2. Basic concept and motion principle

The compliant structure of continuum robots is an inherent feature that enables versatile motion in confined and unstructured environments [30]. Previous research has demonstrated that continuum robots exhibit superior manipulation performance in extreme circumstances compared to traditional rigid-link robots. However, the majority of deployed continuum robots are designed at micro or small scales to maintain high stiffness and constrain their shape, allowing them to align more closely with theoretical models [31, 32]. As the dimensions of a continuum robot increase to the order of one meter, the shape deformation becomes increasingly nonlinear, significantly decreasing controllability due to large deflections and vibrations. This effect is particularly pronounced when external forces are applied to the robot. One approach to enhancing controllability is to reinforce the structural stiffness; however, this method often results in a trade-off between dexterity and flexibility.

To address the challenges of maintaining both stiffness and softness in continuum robots, our previous work proposed a hybrid concept called the "switchable rigid-continuum robot" (SRC-Bot) [33]. The SRC-Bot can transition between rigid and continuum configurations by locking or unlocking its guiders, as illustrated in Figure 1. While it is theoretically possible to configure a functional robot or manipulator using a single SRC-Bot, practical limitations arise due to insufficient degrees of freedom (DoF) and restricted motion range. Consequently, the SRC-Bot is envisioned as a potential dexterous end effector that can be integrated with various industrial robots, such as articulated, SCARA, or delta robots, depending on the specific task requirements (Figure 1(a)). The integration of an SRC-Bot with industrial robots offers several advantages. It can enhance compliance and flexibility, enabling these robots to overcome challenges and perform tasks in narrow, confined spaces or extremely limited dimensional environments. This hybrid approach combines the precision and strength of traditional industrial robots

https://doi.org/10.1017/S0263574724001735 Published online by Cambridge University Press

with the adaptability and dexterity of continuum robots, potentially expanding the application range of robotic systems in complex environments.

2.1. Structure design and scenarios

Figure 1(a) illustrates the global design of the SRC-Bot, which comprises three main components arranged in series: guiders, elastic chambers, and driven cables. The elastic chamber, the core element, is constructed using thermoplastic polyurethane material via 3D printing technology, imparting exceptional deformability and softness to the SRC-Bot. A standard unit consists of two guiders and a chamber, with five such units interconnected by three cables to form a complete assembly.

This structural design enables the SRC-Bot to operate in two distinct configurations, each offering unique advantages:

1. Continuum Status: when the guiders are unlocked from adjacent units, the SRC-Bot functions as a continuum robot. This configuration provides favorable compliance and flexibility, allowing for deformability and enhanced interaction with objects in complex environments. However, this mode results in reduced load-bearing capacity.
2. Rigid Status: by locking the guiders together, the SRC-Bot transforms into a rigid body. This configuration significantly enhances stiffness, enabling more stable handling of heavier objects. The trade-off in this mode is reduced deformability.

The ability to switch between these two operational modes allows the SRC-Bot to adapt to specific task demands, facilitating dexterous manipulation of objects in confined spaces. This dual-mode functionality combines the advantages of both continuum and rigid robots, potentially expanding the range of applications in complex and constrained environments.

2.2. Switchable motion principle

The SRC-Bot has been designed and implemented to address more complex tasks in unstructured environments. Its key feature is the ability to switch configurations, allowing it to acquire higher deformability or load capacity as required by specific tasks. The most distinctive design element is the skewed slot structure at the edge of each guider. This innovative feature enables the upside edge of one guider to lock with the downside edge of another when the cable is tensioned, resulting in two adjacent guiders being completely locked together to form a rigid status, as illustrated in Figure 1(b). Furthermore, the axial rotation of adjacent guiders is constrained by the cables and skewed slot structure, enhancing the stability of the rigid configuration. Conversely, the SRC-Bot can transition from a rigid to a continuum status by releasing the cable and separating the adjacent guiders.

This switchable status confers two distinct features to the SRC-Bot: higher deformability in the soft (continuum) body configuration and greater load capacity in the rigid body configuration. The advantage of this switchable status lies in its versatility, allowing the robot to adapt to various task requirements. However, it is important to note that when the SRC-Bot is configured for increased stiffness to carry heavier objects, there is a corresponding reduction in the number of DoF.

3. Kinematics

The field of kinematics of continuum robots has seen significant advancement in the past decade, with a particular focus on the fundamental deformation behavior. In this context, the posture of continuum robots is typically approximated as a circular arc shape with constant curvature. However, the condition for holding constant curvature assumes that the stiffness of continuum robots is large enough to prevent the deflection caused by the gravity effect, otherwise, the shape of continuum robots cannot be assumed

https://doi.org/10.1017/S0263574724001735 Published online by Cambridge University Press

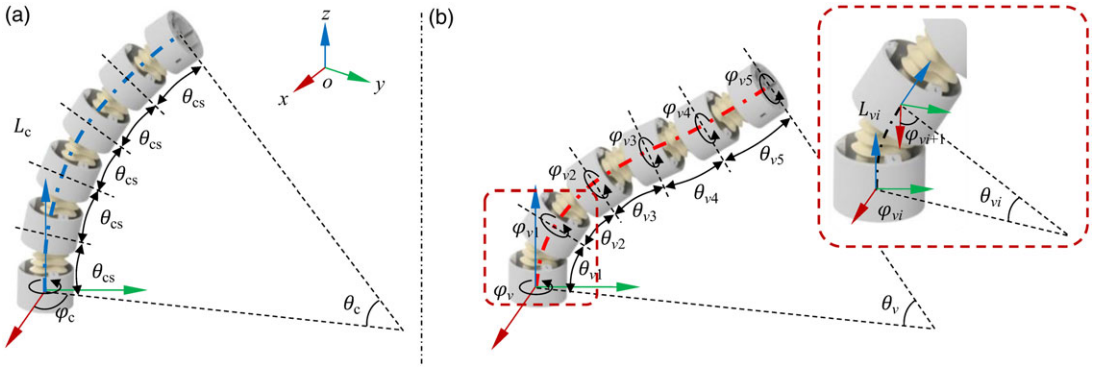

Figure 2. *Kinematic analysis of SRC-Bot: (a) Constant curvature posture, where L_c is the total length, φ_c and θ_c are the rotation and bending angle of the tip, θ_{cs} is the bending angle of each segment; (b) variable curvature posture, where L_{vi}, φ_{vi}, and θ_{vi} are the length, rotation angle, and bending angle of each segment, respectively, i is from 1 to 5, θ_v is the bending angle of the tip, φ_v is the rotation angle of the bottom guider.*

as an arc with constant curvature. Hence, a suitable way to acquire an accurate kinematic model is by utilizing the variable curvature assumption. In this section, the kinematics of continuum robots is established by combining the method of constant and variable curvature.

3.1. Constant curvature shape

Figure 2 illustrates two schematic diagrams of the kinematic shape by using constant and variable curvature configurations for identifying the deformed shape of continuum robots kinematically. As shown in Figure 2(a), the most general method is to assume the posture (dark blue central curve) of continuum robots as a constant circular arc, in which the bending angle θ_{cs} between each cable guider is the same, and there is no relative rotational motion between each guider, therefore, the basic kinematic translation $\mathbf{P}_c \in \mathbb{R}^{3\times1}$ is expressed as

$$\boldsymbol{P}_c = \begin{bmatrix} x_c \\ y_c \\ z_c \end{bmatrix} = \begin{bmatrix} \frac{L_c}{\theta_c}\left(1-\cos\left(\theta_c\right)\right)\cos\left(\varphi_c\right) \\ \frac{L_c}{\theta_c}\left(1-\cos\left(\theta_c\right)\right)\sin\left(\varphi_c\right) \\ \frac{L_c}{\theta_c}\sin\left(\theta_c\right) \end{bmatrix} \tag{1}$$

where (x_c, y_c, z_c) is the coordinate of end position, and θ_c, φ_c, and L_c are the bending angle, rotation angle, and length of the shape of continuum robot as shown in Figure 2(a). The special case for SRC-bot is that the length is capable of changing to switch the configuration from rigid status to continuum status, and vice versa. The central coordinates of each guider can be calculated by discretizing the continuum robot with the same bending angle, rotation angle, and length based on the number of the guiders.

The revolute motion matrix $\mathcal{M}_{ci} \in \mathbb{R}^{3\times3}$ contributed by bending angle and rotation angle could be expressed as

$$\mathcal{M}_{ci} = \mathcal{R}_{cz}(\varphi_{ci})\mathcal{R}_{cy}(\theta_c) \tag{2}$$

where $\mathcal{R}_{cz}$ and $\mathcal{R}_{cy}$ are the rotation matrix with respect to the z-axis and y-axis, respectively, which could be constituted by

https://doi.org/10.1017/S0263574724001735 Published online by Cambridge University Press

$$\begin{cases} \mathcal{R}_{cz}(\varphi_c) = \begin{bmatrix} \cos(\varphi_c) & -\sin(\varphi_c) & 0 \\ \sin(\varphi_c) & \cos(\varphi_c) & 0 \\ 0 & 0 & 1 \end{bmatrix} \\ \mathcal{R}_{cy}(\theta_c) = \begin{bmatrix} \cos(\theta_c) & 0 & \sin(\theta_c) \\ 0) & 1 & 0 \\ -\sin(\theta_c) & 0 & \cos(\theta_c) \end{bmatrix} \end{cases} \tag{3}$$

3.2. Variable curvature shape

In accordance with the kinematics of constant curvature, the fundamental motion behavior of SRC-Bot can be reflected only when the stuffiness of the continuum robot is sufficiently large to eliminate the greatest deflection. Nevertheless, the shape approximation of the constant curvature method becomes increasingly inaccurate as the dimensional scale of the continuum robot is increased, or as the deflection caused by gravity and external forces becomes more significant.

Therefore, a discretization method is proposed in this section to acquire a more precise kinematic model by assuming the deformation of the continuum robot as a variable curvature shape as shown in Figure 2(b). Apart from the constant curvature method, the bending angle θ_{vi} between each adjacent guider, the rotation angle φ_{vi} of each guider, and the discretized arc length L_{vi} are defined as a variable for obtaining a deformed shape, in which the curvature evenly changes along the central axis. Consequently, the kinematics with variable curvature can be derived and established based on the series system configuration by employing the transformation matrix that incorporates translation and revolute motion.

The relative translation $\mathbf{P}_{vi} \in \mathbb{R}^{3\times1}$ of each discretized segment in local cartesian coordinate system is

$$\mathbf{P}_{vi} = \begin{bmatrix} x_{vi} \\ y_{vi} \\ z_{vi} \end{bmatrix} = \begin{bmatrix} \frac{L_{vi}}{\theta_{vi}}(1-\cos(\theta_{vi}))\cos(\varphi_{vi}) \\ \frac{L_{vi}}{\theta_{vi}}(1-\cos(\theta_{vi}))\sin(\varphi_{vi}) \\ \frac{L_{vi}}{\theta_{vi}}\sin(\theta_{vi}) \end{bmatrix} \tag{4}$$

The revolute motion matrix $\mathcal{M}_{vi} \in \mathbb{R}^{3\times1}$ is as

$$\mathcal{M}_{vi} = \mathcal{R}^z_{vi}(\varphi_c)\mathcal{R}^y_{vi}(\theta_c) \tag{5}$$

where $\mathcal{R}^z_{vi}$ and $\mathcal{R}^y_{vi}$ are the rotation matrix with respect to z-axis and y-axis, respectively, hence, the homogeneous transformation matrix $\mathbf{T}_{vi}$ could be constituted as

$$\mathbf{T}_{vi} = \begin{bmatrix} \mathcal{M}_{vi} & \mathbf{P}_{vi} \\ 0 & 1 \end{bmatrix} \tag{6}$$

According to the discretization method, the global translation $\mathbf{P}_i \in \mathbb{R}^{3\times1}$ of each guider respect to base coordinate system is

$$\begin{bmatrix} \mathbf{P}_i \\ 1 \end{bmatrix} = \begin{bmatrix} x_i \\ y_i \\ z_i \\ 1 \end{bmatrix} = \left(\prod_1^{i-1} \mathbf{T}_{vi}\right) \begin{bmatrix} \mathbf{P}_{vi} \\ 1 \end{bmatrix}, (i = 1, 2, 3 \cdots n) \tag{7}$$

where n is the total number of the guiders, as a result, the deformed shape of the whole body with variable curvature could be expressed based on Eq. (7).

Although the kinematics model with the assumption of variable curvature is able to accurately describe the behavior of deformation of the continuum robot, the discretized parameters, such as angle and length changing caused by external force and gravity effect need to be specified in terms of the

https://doi.org/10.1017/S0263574724001735 Published online by Cambridge University Press

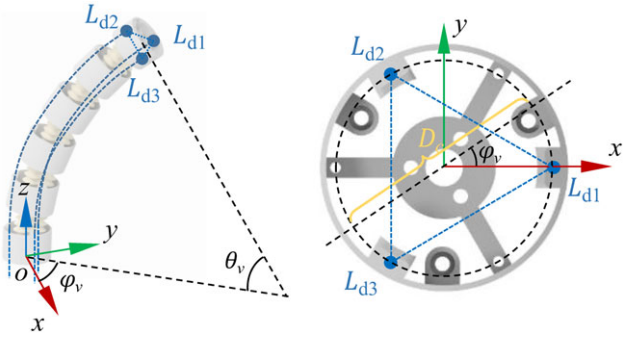

Figure 3. *Driven space analysis of SRC-Bot, where L_{di} is the length of each driven cable, i is from 1 to 3. θ_v is the bending angle of the tip, φ_v is the rotation angle of the bottom guider.*

mechanics analysis. Moreover, the controllable DoF is still three, two orientations and one translation of the tip guider, denoted by $(\theta_v, \varphi_v, L_v)$ which is the sum of the discretized bending angle, rotation angle, and the arc length.

3.3. Driven kinematics

By involving the bending angle, rotation angle, and length, the relationship between workspace (x_v, y_v, z_v) and joint space $(\theta_v, \varphi_v, L_v)$ is established based on the variable curvature kinematic model. However, the implementation of driving the orientation and length depends on the control of each cable length through the actuation motors. Hence, the kinematic mapping between the joint space $(\theta_v, \varphi_v, L_v)$ and the driving space L_{di} needs to be modeled.

In this paper, the continuum robot is driven by three cables distributed around the center of the guider at 120 degrees as shown in Figure 3. Driven space $\{L_{dj}, j = 1, 2, 3\}$ refers to the relation between the cable length and the joint space parameters, which can be expressed as Eq. (8).

$$\begin{cases} L_{d1} = L_v + \frac{D_c}{2}\theta_v \cos(\varphi_v) \\ L_{d2} = L_v + \frac{D_c}{2}\theta_v \cos\left(\varphi_v + \frac{2\pi}{3}\right) \\ L_{d3} = L_v + \frac{D_c}{2}\theta_v \cos\left(\varphi_v - \frac{\pi}{3}\right) \end{cases} \tag{8}$$

where D_c is the diameter of the circle where the cable holes are located. The length of each cable is calculated when the joint space parameters are specified. Similar to the computation of driven space parameters, the shape coordinate (x_{vi}, y_{vi}, z_{vi}) in workspace can be obtained when $(\theta_v, \varphi_v, L_v)$ are given. In addition, the simultaneous kinematics, such as the relationship of velocity or angular velocity, could be established by using the Jacobian matrix based on the partial differential equation derived from the basic kinematic model, as Eqs. (1), (4) and (8).

4. Dynamics of SRC-Bot

Dynamic behavior represents the most significant intrinsic property, as it significantly reflects and influences the movability, stability, and controllability of the robot, particularly in the case of continuum robots comprising soft/elastic and structural components. This section presents a comprehensive dynamics modeling approach for analyzing the dynamic response of SRC-Bot, which involves external forces, gravity, and actuation friction. The shape deformation and motion are described through a discretization method based on Newton's second law in a spatial dimension.

https://doi.org/10.1017/S0263574724001735 Published online by Cambridge University Press

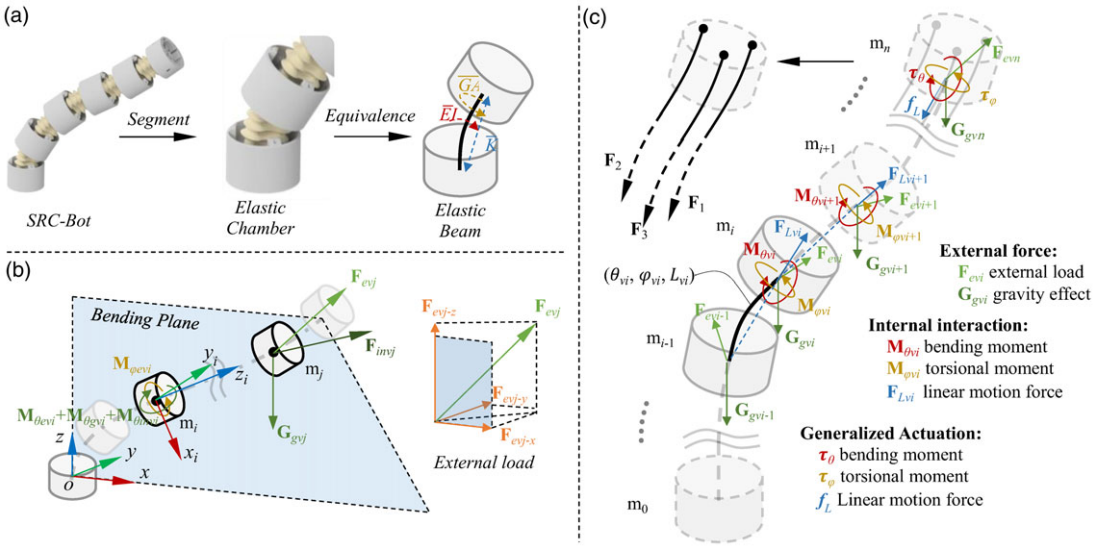

Figure 4. *Structure equivalence and dynamics analysis of SRC-Bot: (a) Equivalence of the segment of SRC-Bot, where $\overline{EI}$ is the bending stiffness, $\overline{GA}$ is the torsional stiffness, and $\overline{K}$ is the linear motion stiffness; (b) moment contributed by external load and gravity, where $\vec{\mathbf{M}}_{\varphi evi}$ and $\vec{\mathbf{M}}_{\theta evi}$ are the moment generated by the external force $\mathbf{F}_{evj}$ in bending and rotation direction, respectively. $\vec{\mathbf{M}}_{\theta gvi}$ is the moment caused by gravity, $\vec{\mathbf{M}}_{\theta invi}$ is the moment owing to the inertia force; (c) mechanics analysis of the segment of SRC-Bot, where $\mathbf{F}_i$ is the force actuated on cables.*

4.1. Structure equivalence and discretization

The variable curvature method in kinematics employs the discretized segments along SRC-Bot as the fundamental unit for analysis. This is illustrated in Figure 4(b), in which the bending angle, rotating angle, and length of each segment undergo dynamic changes due to the combined effects of actuation force, gravity, and external force. Furthermore, the flexibility and compliance of each discretized segment of SRC-Bot originated from the design of an elastic chamber; therefore, the bending, rotating, and elongating motion are all significantly influenced by the stiffness property of the chamber. However, the elastic chamber is an irregularly shaped structure with a corrugated shell, and it is difficult to theoretically calculate the stiffness with respect to bending, rotating, and elongating motion. Hence, an equivalence method is supposed to be used for replacing the elastic chamber with an equivalent elastic beam by defining three equivalent stiffnesses: bending stiffness $\overline{EI}$, torsional stiffness $\overline{GA}$, and linear motion stiffness $\overline{K}$ as shown in Figure 4(a). It is observed that the direction of the linear motion stiffness is assumed to be aligned with the chordal direction of the bending curve, while the torsional stiffness is situated around the central axis along the shape of the segments.

For analyzing the dynamics behavior, SRC-Bot is considered to be a series system that is discretized into multiequivalent beam segments connected. Consequently, the spatial shape of each segment is deformed by internal interaction and external force. The internal interaction indicates that the force and moment are mutually transmitted between each adjacent discretized segment, for example, bending moment, torsional moment, and linear force contributed by the most adjacent segments. The external force including the gravity effect, actuation force, and the external load are all involved in acquiring a comprehensive dynamics model as shown in Figure 4(b). In particular, previous research has predominantly focused on external loads acting at the end of continuum robots. In contrast, this paper considers the external load acting on the body (each guider) in order to analyze the deformable behavior of SRC-Bot when in contact with external objects.

https://doi.org/10.1017/S0263574724001735 Published online by Cambridge University Press

In addition, the generalized actuation forces with respect to bending, rotating, and linear motion, respectively, are applied to the end guider of SRC-Bot, which could be calculated by utilizing the force actuated from the cables based on the Jacobian matrix.

4.2. Bending, elongating, and rotating motion equation

SRC-Bot has three DoF, namely bending, rotating, and elongating, which enable the tip end to reach a specific spatial position within the workspace. In the context of kinematics, the discretization concept allows for the analysis of each discretized segment to have three DoF. This implies that the dynamic spatial motion, including bending, rotation, and elongation, of each segment should be specifically analyzed in terms of the equivalent method as previously mentioned.

In this work, three assumptions lead to the deduction of the dynamics model: 1) the curvature of each discretized segment is constant but different from each other; 2) the elastic chamber is simplified as a beam with the corresponding structural property; and 3) the stiffness and damping are independently separated into three dimensions in joint space related to bending, elongation, and rotation.

Bending is the most significant DoF and basic behavior of continuum robots that influence the performance and shape deformability of SRC-Bot. As illustrated in Figure 4(c), the orientation in bending direction of the guider i where $i = \{1, 2, \ldots, n-1\}$ could be described as

$$J_{\theta vi}\dot{\omega}_{\theta vi} = \mathbf{M}_{\theta vi} + \mathbf{M}_{\theta evi} + \mathbf{M}_{\theta gvi} + \mathbf{M}_{\theta invi} \tag{9}$$

where $J_{\theta vi}$ is the moment of inertia of the guider relative to the y axis in bending plane, $\omega_{\theta vi}$ is the bending angular acceleration relative to the base coordinates, $\mathbf{M}_{\theta vi}$ is the internal moment caused by upper adjacent segment due to the elastic bending deformation, and $\mathbf{M}_{\theta evi}$ and $\mathbf{M}_{\theta gvi}$ are the moments in bending axis direction generated by the external load and gravity, respectively. In addition, $\mathbf{M}_{\theta invi}$ is the moment caused by the inertia force. According to the pure bending and damping, $\mathbf{M}_{\theta vi}$ could be expressed as

$$\mathbf{M}_{\theta vi} = \frac{\overline{EI}\,(\theta_{vi+1} - \theta_{vi})}{L_{vi}} + d_\theta\left(\dot{\theta}_{vi+1} - \dot{\theta}_{vi}\right) \tag{10}$$

where d_θ is the damping coefficient respected to bending motion. From Eq. (10), the internal moment is generated by the difference of bending angle and angular velocity between two adjacent guiders. In this model, the external load $\mathbf{F}_{\theta evi}$ is not only acting on the tip of SRC-Bot but also acting on other guiders. Therefore, the total moment $\mathbf{M}_{tevi}$ generated by the external load could be calculated as

$$\overrightarrow{\mathbf{M}}_{tevi} = \sum_{j=i+1}^{n} \overrightarrow{\mathbf{r}}_j \times \overrightarrow{\mathbf{F}}_{evj} \tag{11}$$

where $\overrightarrow{r}$ is the vector from central point of guider i to guider j, which is expressed by Eq. (12) based on the kinematics, and $\mathbf{F}_{evj}$ is the external load acting on the guider j.

$$\begin{cases} \overrightarrow{\mathbf{r}}_j = \overrightarrow{\boldsymbol{P}}_j - \overrightarrow{\boldsymbol{P}}_i = \left(x_j - x_i\right)\mathbf{I} + \left(y_j - y_i\right)\mathbf{J} + \left(z_j - z_i\right)\mathbf{K} \\ \overrightarrow{\mathbf{F}}_{evj} = \mathrm{F}_{x-evj}\mathbf{I} + \mathrm{F}_{y-evj}\mathbf{J} + \mathrm{F}_{z-evj}\mathbf{K} \end{cases} \tag{12}$$

F_{x-evj}, F_{y-evj}, and F_{z-evj} are the external load in x, y, and z directions respected to global coordinates. Hence, the total moment $\mathbf{M}_{tevi}$ contributed by the external load is derived by substituting Eq. (12) into Eq. (11) as

$$\overrightarrow{\mathbf{M}}_{tevi} = \sum_{j=i+1}^{\mathrm{n}} \left(\begin{vmatrix} \mathbf{I} & \mathbf{J} & \mathbf{K} \\ x_j - x_i & y_j - y_i & z_j - z_i \\ \mathrm{F}_{x-evj} & \mathrm{F}_{y-evj} & \mathrm{F}_{z-evj} \end{vmatrix} \right) \tag{13}$$

https://doi.org/10.1017/S0263574724001735 Published online by Cambridge University Press

Subsequently, the moment $\mathbf{M}_{\theta evi}$ is the projection of $\mathbf{M}_{tevi}$ on bending axis $\overrightarrow{y}_i$ of i^{th} guider as

$$\overrightarrow{\mathbf{M}}_{\theta evi} = \overrightarrow{\mathbf{M}}_{tevi} \cdot \overrightarrow{\boldsymbol{y}}_i = \overrightarrow{\mathbf{M}}_{tevi} \cdot \left(\prod_{1}^{i} \mathcal{M}_{vi} \begin{bmatrix} 0 \\ 1 \\ 0 \end{bmatrix} \right) \tag{14}$$

Furthermore, the gravity effect generates another moment $\mathbf{M}_{tgvi}$ acting on i^{th} guider is

$$\overrightarrow{\mathbf{M}}_{tgvi} = \sum_{j=i+1}^{n} \overrightarrow{\mathbf{r}}_j \times \overrightarrow{\mathbf{G}}_{gvj} \tag{15}$$

where $\overrightarrow{\mathbf{G}}_{gvj}$ is the gravity of j^{th} guider and could be computed as

$$\overrightarrow{\mathbf{G}}_{gvj} = m_j g \mathbf{K} \tag{16}$$

Hence, the total moment caused by the gravity of each guider is obtained by substituting Eq. (16) into Eq. (15) as

$$\overrightarrow{\mathbf{M}}_{\text{tevi}} = \sum_{j=i+1}^{\text{n}} \left(\begin{vmatrix} \mathbf{I} & \mathbf{J} & \mathbf{K} \\ x_j - x_i & y_j - y_i & z_j - z_i \\ 0 & 0 & m_j g \end{vmatrix} \right) \tag{17}$$

Furthermore, the moment $\overrightarrow{\mathbf{M}}_{\theta gvi}$ is the projection of $\overrightarrow{\mathbf{M}}_{tgvi}$ that could be derived as

$$\overrightarrow{\mathbf{M}}_{\theta gvi} = \overrightarrow{\mathbf{M}}_{tgvi} \cdot \overrightarrow{\boldsymbol{y}}_i = \overrightarrow{\mathbf{M}}_{tgvi} \cdot \left(\prod_{1}^{i} \mathcal{M}_{vi} \begin{bmatrix} 0 \\ 1 \\ 0 \end{bmatrix} \right) \tag{18}$$

Besides the external load, the inertia force $\overrightarrow{\mathbf{F}}_{invi}$ generated by the linear acceleration $\overrightarrow{\boldsymbol{a}}_i$, including tangential $\overrightarrow{\boldsymbol{a}}_{ti}$ and centripetal acceleration $\overrightarrow{\boldsymbol{a}}_{ci}$ of each guider influences the dynamic behavior, which could be derived as

$$\vec{\mathbf{F}}_{invi} = -\mathrm{m}_i(\vec{\boldsymbol{a}}_{ti} + \vec{\boldsymbol{a}}_{\perp i}) = -\mathrm{m}_i \left(\left(\vec{\dot{\boldsymbol{\omega}}}_{\theta i} + \vec{\dot{\boldsymbol{\omega}}}_{\varphi i} \right) \times \vec{\mathbf{r}}_i + \left| \vec{\boldsymbol{\omega}}_{\theta i} + \vec{\boldsymbol{\omega}}_{\varphi i} \right|^2 \cdot \vec{\mathbf{r}}_i \right) \tag{19}$$

Similar to moment derivation of external load, the total moment $\overrightarrow{\mathbf{M}}_{tinvi}$ acting on guider i could be expressed as

$$\overrightarrow{\mathbf{M}}_{\theta invi} = \left(\sum_{j=i+1}^{n} \overrightarrow{\mathbf{r}}_j \times \overrightarrow{\mathbf{F}}_{invj} \right) \cdot \left(\prod_{1}^{i} \mathcal{M}_{vi} \begin{bmatrix} 0 \\ 1 \\ 0 \end{bmatrix} \right) \tag{20}$$

Consequently, the angular acceleration of bending motion is completely expressed by

$$\dot{\omega}_{\theta vi} + \frac{\overline{EI}}{J_{\theta vi} L_{vi}} (\theta_{vi} - \theta_{vi+1}) + \frac{d_\theta}{J_{\theta vi}} (\dot{\theta}_{vi} - \dot{\theta}_{vi+1}) = \frac{\tau_{\theta egvi}}{J_{\theta vi}} \tag{21}$$

where $\tau_{\theta egvi}$ is the absolute value of the sum of $\overrightarrow{\mathbf{M}}_{\theta gvi}$, $\overrightarrow{\mathbf{M}}_{\theta evi}$, and $\overrightarrow{\mathbf{M}}_{\theta invi}$.

As the mechanical design of the actuation system, three cables are fixed with the top guider n and steer SRC-Bot through the motors, which means the actuation force is only acting on the top guider. Therefore, a generalized actuation moment τ_θ relative to bending motion is applied to the dynamic motion equation of guider n, and the final motion equation of bending is as

$$\begin{cases} \dot{\omega}_{\theta vi} + \frac{\overline{EI}}{J_{\theta vi} L_{vi}} (\theta_{vi} - \theta_{vi+1}) + \frac{d_\theta}{J_{\theta vi}} \left(\dot{\theta}_{vi} - \dot{\theta}_{vi+1} \right) = \frac{\tau_{\theta egvi}}{J_{\theta vi}} \\ \qquad\qquad\qquad\qquad\qquad\qquad\qquad\qquad\qquad\qquad , i = 1, 2, \cdots, n-1 \\ \dot{\omega}_{\theta vn} + \frac{\overline{EI}}{J_{\theta vn} L_{vn}} \theta_{vn} + \frac{d_\theta}{J_{\theta vn}} \dot{\theta}_{vn} = \frac{\tau_{\theta egvn} + \tau_\theta}{J_{\theta vn}} \end{cases} \tag{22}$$

Equation (21) and (22) are the complete dynamics equation of bending motion, in which the θ_{vi}, θ_{vn}, $\dot{\theta}_{vi}$, and $\dot{\theta}_{vn}$ are relative value reference to i^{th} the coordinates, and $\dot{\omega}_{\theta vi}$, $\dot{\omega}_{\theta vn}$, a_{ti}, and a_{ci} are global value

https://doi.org/10.1017/S0263574724001735 Published online by Cambridge University Press

reference to the base coordinates. Linear motion is an essential DoF of SRC-Bot, with which the robot could elongate and stretch to a specific length, especially for locking and unlocking each adjacent guider to switch configuration from continuum status to rigid status.

The linear motion assumes that the motion direction is along the chordal direction of the bending curve, and is described as

$$m_i a_{Lvi} = -\overline{K}(C_{vi} - C_0) - b_L \dot{C}_{vi} + \overline{K}(C_{vi+1} - C_0) + d_L \dot{C}_{vi+1} + \mathrm{G}_{Lgvi} + \mathrm{F}_{Levi} \tag{23}$$

where a_{Lvi} is the acceleration along the chordal direction, C_0 is the chord length with a natural arc length of the elastic chamber, and C_{vi} is the actual chord length between $i-1^{th}$ and i^{th} guider. The relation between the chord length and arc length is as

$$C_{vi} = \frac{2L_{vi}}{\theta_{vi}} \sin\left(\frac{\theta_{vi}}{2}\right) \tag{24}$$

Moreover, $\dot{C}_{vi}$ is the changing rate of the chord length, d_L is the damping coefficient of the linear motion.

Similar to bending motion, the gravity effect $\vec{\mathbf{G}}_{Levj}$ and external force $\vec{\mathbf{F}}_{Levi}$ are involved into the dynamic equation. Hence, the external force acting on ith guider is expressed as the projection of $\vec{\mathbf{F}}_{Levi}$ along the chordal direction as

$$\vec{\mathbf{F}}_{Levi} = \frac{\vec{\mathbf{F}}_{evi} \cdot (\vec{\boldsymbol{P}}_{i+1} - \vec{\boldsymbol{P}}_i)}{\left\|\vec{\boldsymbol{P}}_{i+1} - \vec{\boldsymbol{P}}_i\right\|} \frac{\vec{\boldsymbol{P}}_{i+1} - \vec{\boldsymbol{P}}_i}{\left\|\vec{\boldsymbol{P}}_{i+1} - \vec{\boldsymbol{P}}_i\right\|} \tag{25}$$

Furthermore, the gravity effect projected on the chordal direction is derived as

$$\vec{\mathbf{G}}_{Lgvj} = \frac{\vec{\mathbf{G}}_{gvj} \cdot (\vec{\boldsymbol{P}}_{i+1} - \vec{\boldsymbol{P}}_i)}{\left\|\vec{\boldsymbol{P}}_{i+1} - \vec{\boldsymbol{P}}_i\right\|} \frac{\vec{\boldsymbol{P}}_{i+1} - \vec{\boldsymbol{P}}_i}{\left\|\vec{\boldsymbol{P}}_{i+1} - \vec{\boldsymbol{P}}_i\right\|} \tag{26}$$

The generalized actuation force f_L is only acting on the top guider, thus the dynamic equation of n^{th} guider is

$$m_n a_{Lvn} = -\overline{K}(C_{Lvn} - C_0) - d_L \dot{C}_{Lvn} + \mathrm{G}_{Lgvn} + \mathrm{F}_{Levn} + f_L \tag{27}$$

$$\begin{cases} a_{Lvi} + \frac{\overline{K}\left(C_{vi} - C_{vi+1}\right)}{m_i} + \frac{d_L\left(\dot{C}_{vi} - \dot{C}_{vi+1}\right)}{m_i} = \frac{f_{Legvi}}{m_i} \\ a_{Lvn} + \frac{\overline{K}(C_{Lvn} - C_0)}{m_n} + \frac{d_L \dot{C}_{Lvn}}{m_n} = \frac{f_{Legvn} + f_L}{m_n} \end{cases}, i = 1, 2 \cdots n-1 \tag{28}$$

where f_{Legvi} is the absolute value of sum of gravity effect $\vec{\mathbf{G}}_{Lgvj}$ and external force $\vec{\mathbf{F}}_{Levi}$.

Except for the bending and linear motion, rotating motion endows SRC-Bot with spatial movability. The general dynamic equation of rotation is described as

$$J_{\varphi vi} \dot{\omega}_{\varphi vi} = \mathbf{M}_{\varphi vi} + \mathbf{M}_{\varphi evi} + \mathbf{M}_{\varphi gvi} + \mathbf{M}_{\varphi invi} \tag{29}$$

where $J_{\varphi vi}$ is the moment of inertia of the guider relative to the z axis, $\dot{\omega}_{\varphi vi}$ is the rotation angular acceleration referred to the base coordinates, $\mathbf{M}_{\varphi vi}$ is the internal moment caused by upper adjacent segment due to the torsional deformation, and $\mathbf{M}_{\varphi evi}$ and $\mathbf{M}_{\varphi gvi}$ are the moments in rotation axis direction generated by the external load and gravity effect, respectively. In addition, $\mathbf{M}_{\varphi invi}$ is the moment caused by the inertia force. The internal moment $\mathbf{M}_{\varphi vi}$ could be described as

$$\mathbf{M}_{\varphi vi} = \frac{\overline{GA}(\varphi_{vi+1} - \varphi_{vi})}{L_{vi}} + d_\varphi(\dot{\varphi}_{vi+1} - \dot{\varphi}_{vi}) \tag{30}$$

https://doi.org/10.1017/S0263574724001735 Published online by Cambridge University Press

where d_φ is the damping coefficient of rotation motion. Subsequently, the moment generated by the external force and gravity is derived similarly to the bending motion as

$$\begin{cases} \overrightarrow{\mathbf{M}}_{\varphi evi} = \overrightarrow{\mathbf{M}}_{tevi} \cdot \vec{z}_i = \overrightarrow{\mathbf{M}}_{tgvi} \cdot \left(\prod_1^i \mathcal{M}_{vi} \begin{bmatrix} 0 \\ 0 \\ 1 \end{bmatrix} \right) \\ \overrightarrow{\mathbf{M}}_{\varphi gvi} = \overrightarrow{\mathbf{M}}_{tgvi} \cdot \vec{z}_i = \overrightarrow{\mathbf{M}}_{tgvi} \cdot \left(\prod_1^i \mathcal{M}_{vi} \begin{bmatrix} 0 \\ 0 \\ 1 \end{bmatrix} \right) \end{cases} \tag{31}$$

The moment $\overrightarrow{\mathbf{M}}_{\varphi evi}$ and $\overrightarrow{\mathbf{M}}_{\varphi gvi}$ are the projection of $\overrightarrow{\mathbf{M}}_{tevi}$ and $\overrightarrow{\mathbf{M}}_{tgvi}$ on z axis, respectively. The inertia force impacted on the rotation is considered in the dynamic equation by using Eqs. (19) and (20), but the revolute axis is z as

$$\vec{\mathbf{M}}_{\varphi invi} = \left(\sum_{j=i+1}^{n} \vec{\mathbf{r}}_j \times \vec{\mathbf{F}}_{invj} \right) \cdot \left(\prod_1^i \mathcal{M}_{vi} \begin{bmatrix} 0 \\ 0 \\ 1 \end{bmatrix} \right) \tag{32}$$

For the n$^t h$ guider, the generalized actuation moment τ_φ is added into the dynamic equation, therefore the complete motion equations relative to the rotation are

$$\begin{cases} \dot{\omega}_{\varphi vi} + \frac{\overline{GA}}{J_{\varphi vi} L_{vi}} (\varphi_{vi} - \varphi_{vi+1}) + \frac{d_\varphi}{J_{\varphi vi}} (\dot{\varphi}_{vi} - \dot{\varphi}_{vi+1}) = \frac{\tau_{\varphi egvi}}{J_{\varphi vi}} \\ \dot{\omega}_{\varphi vn} + \frac{\overline{GA}}{J_{\varphi vn} L_{vn}} \varphi_{vn} + \frac{d_\varphi}{J_{\varphi vn}} \dot{\varphi}_{vn} = \frac{\tau_{\varphi egvn} + \tau_\varphi}{J_{\varphi vn}} \end{cases} , i = 1, 2, \ldots, n-1 \tag{33}$$

where $\tau_{\varphi egvi}$ is the sum of absolute value of $\overrightarrow{\mathbf{M}}_{\varphi evi}$ and $\overrightarrow{\mathbf{M}}_{\varphi gvi}$.

Finally, by using Eqs. (22), (28), and (33), the dynamic motion of SRC-Bot relative to bending, elongation, and rotation could be described and established with corresponding actuation moment and force.

4.3. Generalized force and friction

In the above section, the dynamic motion is derived by using Newton's second law, in which the deformation is described in three dimensions as a joint space, bending, elongation, and rotation actuated by three generalized forces and moment.

In driven kinematics, the relationship between the joint space parameters $(\theta_v, \varphi_v, L_v)$ and driving space parameters $\{L_{dj}, j = 1, 2, 3\}$ is expressed as Eq. (8). Thus, the generalized actuation force and moment could be derived as

$$\begin{bmatrix} \tau_\theta \\ \tau_\varphi \\ f_L \end{bmatrix} = \begin{bmatrix} \sum_{i=0}^{3} \frac{\partial L_{di}}{\partial \theta_v} {}^n\mathrm{F}_i \\ \sum_{i=0}^{3} \frac{\partial L_{di}}{\partial \theta_v} {}^n\mathrm{F}_i \\ \sum_{i=0}^{3} \frac{\partial L_{di}}{\partial \theta_v} {}^n\mathrm{F}_i \end{bmatrix} = \mathbf{J}_d \begin{bmatrix} {}^n\mathrm{F}_1 \\ {}^n\mathrm{F}_2 \\ {}^n\mathrm{F}_3 \end{bmatrix} \tag{34}$$

where $\mathbf{J}_d$ is the Jacobian matrix derived by differentiating Eq. (8) respective to θ_v, φ_v, and L_v, ${}^n\mathrm{F}_i$ is the actuation force transmitted from the motor acting on the nth guider. Inversely, the required actuation force ${}^n\mathrm{F}_i$ is calculated by defining the generalized actuation force and moment.

$$\begin{bmatrix} {}^n\mathrm{F}_1 \\ {}^n\mathrm{F}_2 \\ {}^n\mathrm{F}_3 \end{bmatrix} = \mathbf{J}_d^{-1} \begin{bmatrix} \tau_\theta \\ \tau_\varphi \\ f_L \end{bmatrix} \tag{35}$$

As the configuration and the actuation mode of SRC-Bot, the cables slide inside the hole of the guiders, the friction is unavoidably generated by the actuation force due to the contact between cables

https://doi.org/10.1017/S0263574724001735 Published online by Cambridge University Press

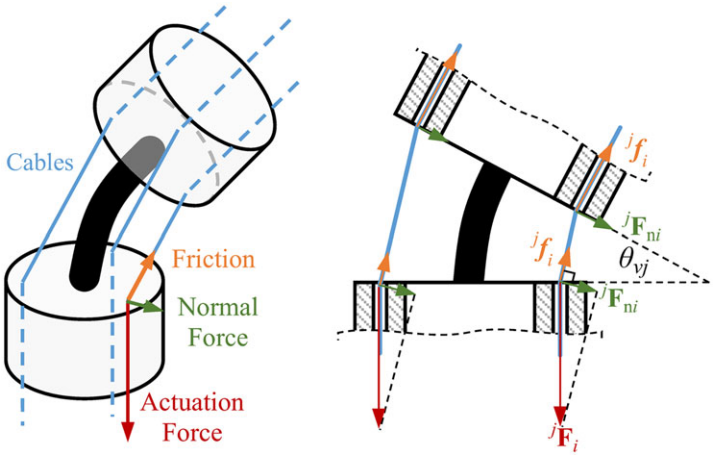

Figure 5. *Fricton force between the cable and guider of SRC-Bot, where* $^{j}F_i$ *is the actuation force,* $^{j}\mathrm{F}_{ni}$ *is the normal force, and* $^{j}f_i$ *is the friction force.*

and guiders. Thus, in this paper, coulomb friction is established into the equation of generalized actuation force as shown in Figure 5. The actuation force is decreased due to the friction when the cable slides across one guider, the force acting on the top guider is decreased by the friction between the cable and other guiders.

To derive the friction function, the mechanics analysis is shown in Figure 5, a normal force $^{j}\mathrm{F}_{ni}$ that is exerted by the surface of the guider on the cables, directed perpendicular to the guider surface, which is contributed from the actuation force $^{j}\mathrm{F}_i$ through the cables across each guider. Therefore, the expression of the friction and the transmitted actuation force could be derived as

$$^{j}f_i = \eta\ ^{j}\mathrm{F}_{ni} = {}^{j}\mathrm{F}_i \cdot \eta \cdot \sin\frac{\theta_{vj}}{2},\ i = 1, 2, 3; j = 1, 2, 3, \cdots, n \tag{36}$$

where η is the friction coefficient between cable and guider. Hence, the force acting on the top guider could be calculated as

$$^{n}\mathrm{F}_i = \mathrm{F}_i \frac{\prod_{j=1}^{n}\left(1 - \eta \cdot \sin\frac{\theta_{vj}}{2}\right)^2}{\left(1 - \eta \cdot \sin\frac{\theta_{vn}}{2}\right)}, i = 1, 2, 3 \tag{37}$$

where F_i is the output force from the motor to the cable. Finally, the generalized force f_L and moment $(\tau_\theta,\ \tau_\varphi)$ could be obtained by defining the value of F_i and bending angle of each segment based on Eqs. (33) and (36).

In summary, the dynamics model is established as Eqs. (22), (28), and (32), in which the gravity and external force are involved in deducing the dynamic deformation and response of SRC-Bot under the actuation force transmitted through the cables from the motors. Moreover, the generalized force and moment in joint space that acts on the top guider are analyzed and derived based on the instantaneous driven kinematics and take account of the corresponding friction generated by the contact between the cables and the guiders.

Consequently, the deformational behavior of bending, elongation, and rotation of SRC-Bot under actuation force and gravity external force has been fully described. This enables the forward and inverse dynamics to be obtained in accordance with the requisite specifications, including behavior validation, motion control, and path planning. It is noted that the equivalent parameters, for example, stiffness ($\overline{EI}$, $\overline{GA}$, and $\overline{K}$), damping coefficients (d_θ, d_φ, and d_L), and friction coefficient η are difficult to be theoretically calculated due to the complexity of the assembled structure and geometric shape, hence a series experiments will conduct to identify the parameter one by one. The structural properties, for

https://doi.org/10.1017/S0263574724001735 Published online by Cambridge University Press

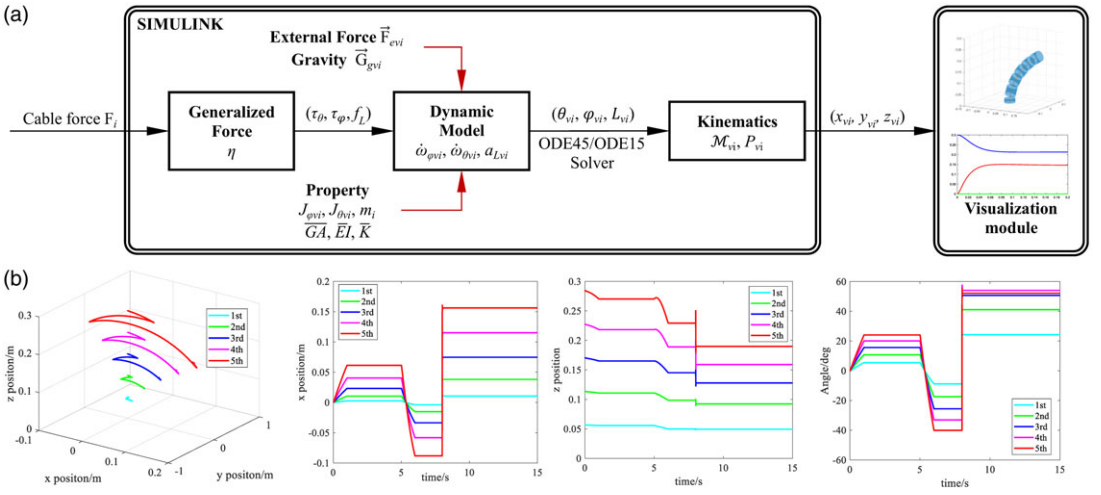

Figure 6. *SIMULATION of SRC-bot: (a) SIMULINK configuration of SRC-Bot based on the proposed dynamics model. As a result, the bending angle, rotation angle, and length of each segment (θ_{vi}, φ_{vi}, L_{vi}) are calculated and inputted to transform matrix $\mathcal{M}_{vi}$ and $\mathbf{P}_{vi}$ for obtaining the coordinates (x_{vi}, y_{vi}, z_{vi}), (b) case for motion response by established simulation.*

example, mass and moment inertia, could be obtained from the CAD model by defining the suitable material parameters.

5. Numerical simulation

In order to verify the proposed theoretical model and clarify the dynamic response, a simulation is carried out using SIMULINK. This involves implementing the mathematical formulas of dynamics proposed in the previous section as a module for numerically simulating the motion of SRC-Bot.

5.1. Simulation and configuration

The proposed dynamics model equations, including motion, generalized force, gravity, and external force, were implemented into the SIMULINK for simulating the dynamic deformation and response of SRC-Bot as shown in Figure 6, which depicts the simulation flow. In accordance with the actuation principle of SRC-Bot, the input is the actuation force of the cable, followed by the generalized force in terms of bending, rotating, and elongating. Subsequently, the acceleration and angular acceleration are calculated by feeding the generalized force and defining the external force, gravity, and property parameters using the internal solver of *ode45* or *ode15*. Thereafter, the bending angle, rotation angle, and length of each discretized segment are integrated from the dynamic model, which is fed into kinematics to obtain the coordinates of each guider in Cartesian space. Finally, a visualization module is established to illustrate the shape deformation of SRC-Bot based on the output coordinates.

5.2. Dynamic simulation

The use of SIMULINK in conjunction with the proposed dynamics model enables the simulation of motions, which can be specified by the user as a function of the actuation force and external force. The resulting posture response includes the position and angle of each guider. Figure 6(b) depicts a typical motion of SRC-Bot simulated based on the SIMULINK, the input actuation force is 7N, 15N, and 15N that activated at 0s and 5s, respectively. Furthermore, a 5N external force acts on the top guider at 8s.

https://doi.org/10.1017/S0263574724001735 Published online by Cambridge University Press

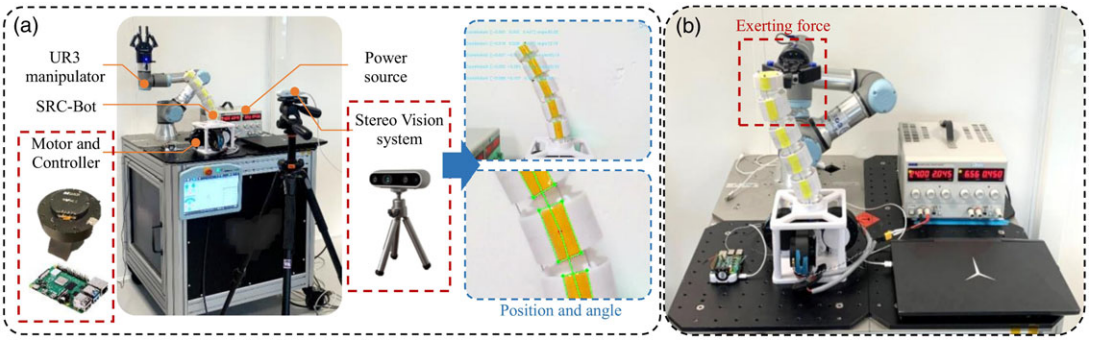

Figure 7. *Experiment setup for validating the model of SRC-Bot: (a) Layout of the experiment setup and deformation tracking; (b) exert the external force by the UR-3 manipulator.*

The total simulation time is 15*s*, and the computational duration is around 800 *ms*, after compiling the model. The simulation results demonstrate the response of trajectory and angle changes of each guider.

6. Experiments

In this section, a prototype of SRC-Bot and an experimental setup were built to validate the theoretical work proposed in the last section. In order to ascertain the precise properties of SRC-Bot, the stiffness parameters were identified through experiments conducted with a single unit guider. Two types of experiments were carried out based on the motion principle and structure characteristics of the continuum robot. First, the behavior response of the forward dynamics is validated by giving an actuation force to each cable. Secondl, the shape deformation under external force is estimated by comparing the results with theoretical predictions.

6.1. Experimental setup

As the illustration in Figure 7(a), the physical structure of SRC-Bot is constructed using 3D-printed components. The rigid components are manufactured from PLA, while the soft components are made from TPU. Three servo motors (RMD-X8 V2, MyActuator) were utilized to steer the robot through three cables, and a controller (Raspberry Pi 4) was used for collaboratively driving the motors based on the desired motion. A UR-3 manipulator is mounted on a platform along with an SRC-Bot, allowing the manipulator to exert an external force on the physical robot and deform its posture as shown in Figure 7(b). Additionally, a stereo vision camera (D435i, Intel) has been set up outside the platform to capture the posture and deformation, including the position and angle of SRC-Bot by identifying the particular label affixed on each guider. The parameters used in experiments are stated in Table I.

6.2. Stiffness identification

In this work, the deformability is generated from the elastic chamber, which is designed with an irregular shape. This makes it challenging to calculate the stiffness in three directions (bending, rotating, and elongation) theoretically. Therefore, a concept of equivalent stiffness is utilized in the dynamics modeling process, which approximates the stiffness as a linear value. To identify the stiffness parameters in 3 directions, a series of experiments were conducted using a single unit fixed on the platform. Figure 8(a)(b)(c) depicts the method of identification experiments. The elongation and bending angle were considered to be the translation and orientation of the end effector. The forces and torques were

https://doi.org/10.1017/S0263574724001735 Published online by Cambridge University Press

Table I. *Results of overloading for 3 experimental setups.*

Parameter	**Value**
Initial length L_0 of each segment	0.057m
Damping coefficients d_θ	0.03
Damping coefficients d_φ	0.03
Damping coefficients d_L	0.03
Moment inertia J_θ	$7.4e^{-6}kg \cdot m^2$
Moment inertia J_φ	$13.1e^{-6}kg \cdot m^2$
Mass of guider m	0.042 kg

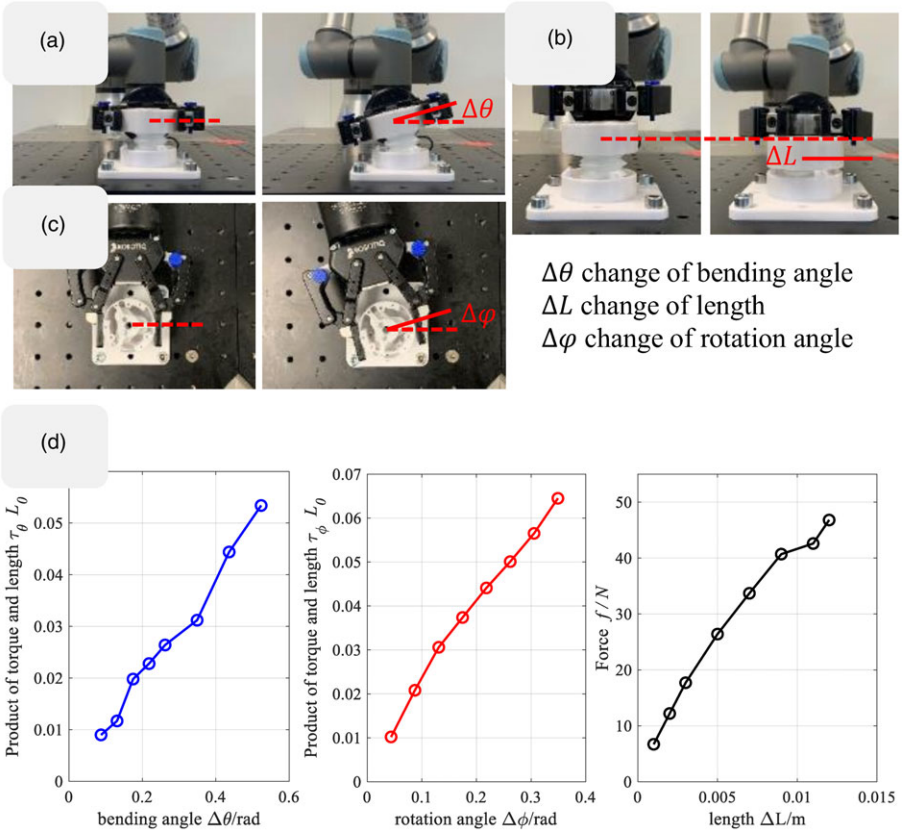

Figure 8. *Equivalent stiffness identification: (a) bending stiffness; (b) linear stiffness; (c) rotation stiffness; (d) identified stiffness curves.*

obtained from the internal sensor of the UR-3 manipulator. Subsequently, the measured data were input into Eq. (38) to obtain the equivalent stiffness of each direction.

$$\begin{bmatrix} \overline{\mathrm{EI}} \\ \overline{\mathrm{GA}} \\ \overline{\mathrm{K}} \end{bmatrix} = \begin{bmatrix} \frac{\tau_\theta L_0}{\Delta\theta} \\ \frac{\tau_\varphi L_0}{\Delta\varphi} \\ \frac{f_L}{\Delta L} \end{bmatrix} \tag{38}$$

https://doi.org/10.1017/S0263574724001735 Published online by Cambridge University Press

The identified results are illustrated in Figure 8(d), each stiffness curve was plotted by using 10 sets of measured data. As the results show, the average equivalent stiffness in the direction of bending, rotating, and elongating is $0.1006\text{N}\cdot\text{m}^2$, $0.2106\text{N}\cdot\text{m}^2$, and 5136 N/m, respectively. Hence, the identified stiffness can be used in the theoretical model of dynamics for simulating the motion of SRC-Bot.

6.3. Shape deformation with actuation force

This experiment examined the response of SRC-Bot under actuation force, comparing the results of simulations with those of experiments. The actuation forces were defined as a constant value with different input times. The position and angle of each guider were then theoretically computed and compared with the experimental results.

Experiments were first conducted to explore the posture deformation and motion of each guider in the xoz plane by applying actuation forces at different times. Figure 9(a) and (b) illustrate a comparison of two experimental cases. The graph depicts the initial and end postures for both experimental and simulated results. The black solid and dotted lines represent the experimental and simulated start postures, respectively, while the dark orange solid and dotted lines represent the corresponding end postures. The experimental coordinates in the xoz plane, including the bending angle and the trajectories of each guider, are plotted with different colors corresponding to the time of measurement for comparison with theoretical values. The notation "nth-e" and "nth-s" (where $n = 1, 2, 3, 4, 5$) represent the experimental and simulated results, respectively, from the bottom guider to the top one.

In the first case, the robot transitioned from a vertical posture to a large negative angle and then back to a small negative angle. The absolute errors (experimental results minus simulated results) are presented in Figure 9(a). In x-direction, the majority of the theoretical outcomes exceed the experimental results, with a maximum error of 12.3 mm. In z-direction, a portion of the theoretical z-positions are less than the experimental outcomes. With respect to bending angles, the fifth guider exhibits the most significant error, exceeding 7°. The errors for the other four guiders predominantly fall within the range of −6° to 2°.

In the second case, the robot was actuated to start from vertical status and bent to a negative angle, then back to a positive angle as shown in Figure 9(b). The maximum error was observed with 4^{th} guider in x direction and 5^{th} in z direction. The bending angle errors are mainly smaller than 5°, but few significant errors were observed as 10° and 15° positively or negatively.

Second, the response of spatial motion under actuation force was both simulated and experimentally tested, as illustrated in Figure 9(c) and (d). In these experiments, the robot initiated movement from a vertical posture, with actuation forces applied sequentially to each cable. Two experimental cases were conducted. Due to limitations of the stereo vision camera system, only the 3-D position of the top guider was sampled. These experimental results were then compared with the simulation outcomes.

Figure 9(c) illustrates the robot's spatial motion sequence. The robot initially exhibited bending with a 0° rotation angle upon actuation of the first cable. Subsequently, the bending angle increased following the actuation of the second and third cables. The maximum IQR error of 5.8 mm was observed in the z-direction. Moreover, the robot initially exhibited a 120° rotation angle upon actuation of the second cable, followed by the subsequent activation of the remaining two cables in a sequential manner. Figure 9(d) shows that the trajectory errors are predominantly below 11.2 mm, indicating that the theoretical simulation effectively reflects the spatial deformation behavior, particularly in capturing changes in the initial moving direction.

This experiment validated the dynamic response and compared it with the theoretical model. Key findings from both in-plane and spatial response experiments include coordinate errors primarily within ±15.1 mm over the experiment duration. Bending angle errors in the in-plane experiments mainly fluctuate within −5° to 5°, although rare results of upper guiders show deviations of approximately 15°.

https://doi.org/10.1017/S0263574724001735 Published online by Cambridge University Press

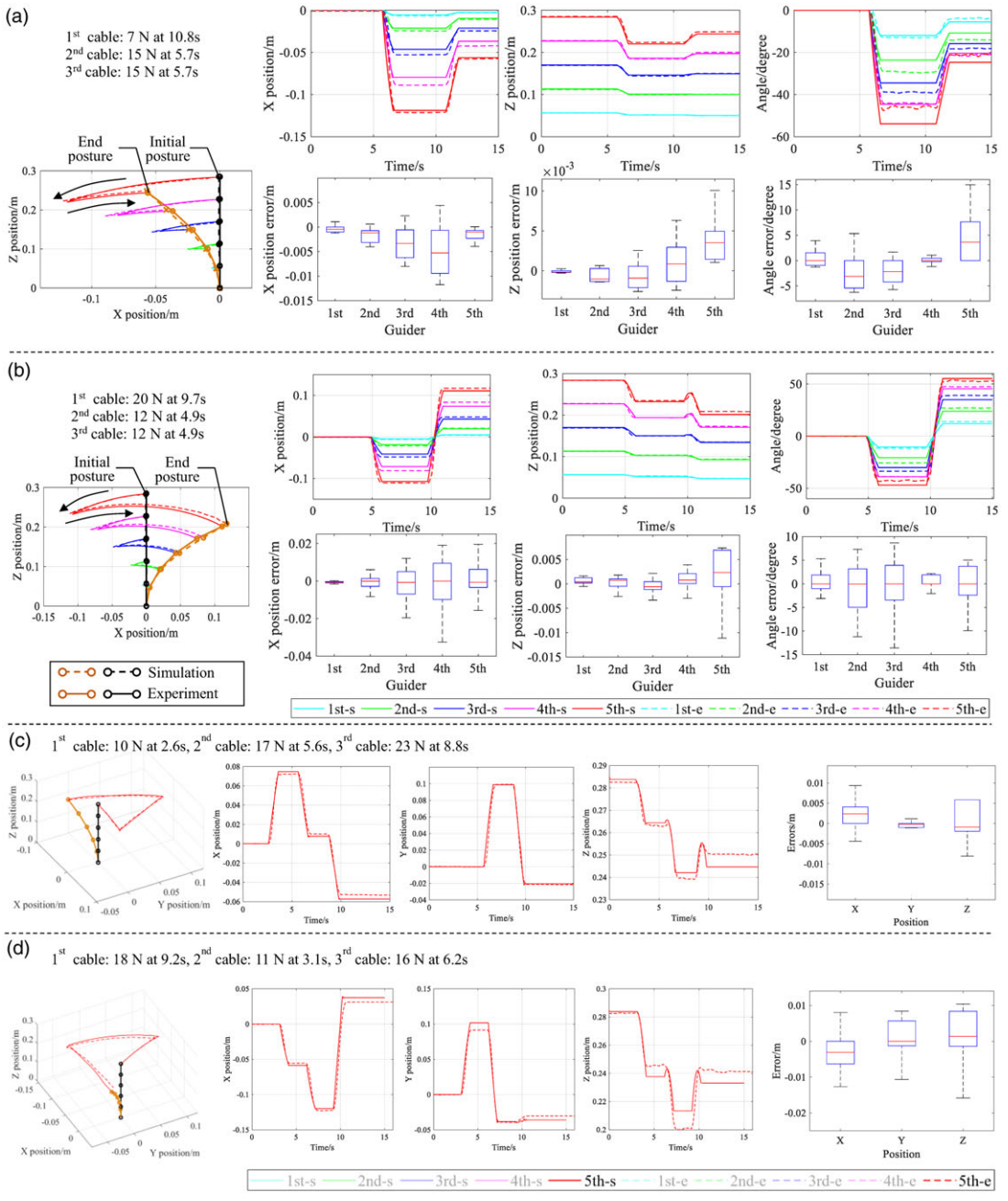

Figure 9. *Illustration of deformation under actuation force, (a)-(d) show the trajectories of each guider and the errors with different forces applied to the cables at specific times.*

The primary sources of discrepancies between experimental and theoretical results are mainly caused by inaccuracies of the stiffness, damping, and friction ratio. The equivalent stiffness used in the model may not fully represent the actual physical value, leading to the deviations of experimental results. Additionally, inaccuracies in damping and friction ratios contribute to discrepancies in the time-domain response.

https://doi.org/10.1017/S0263574724001735 Published online by Cambridge University Press

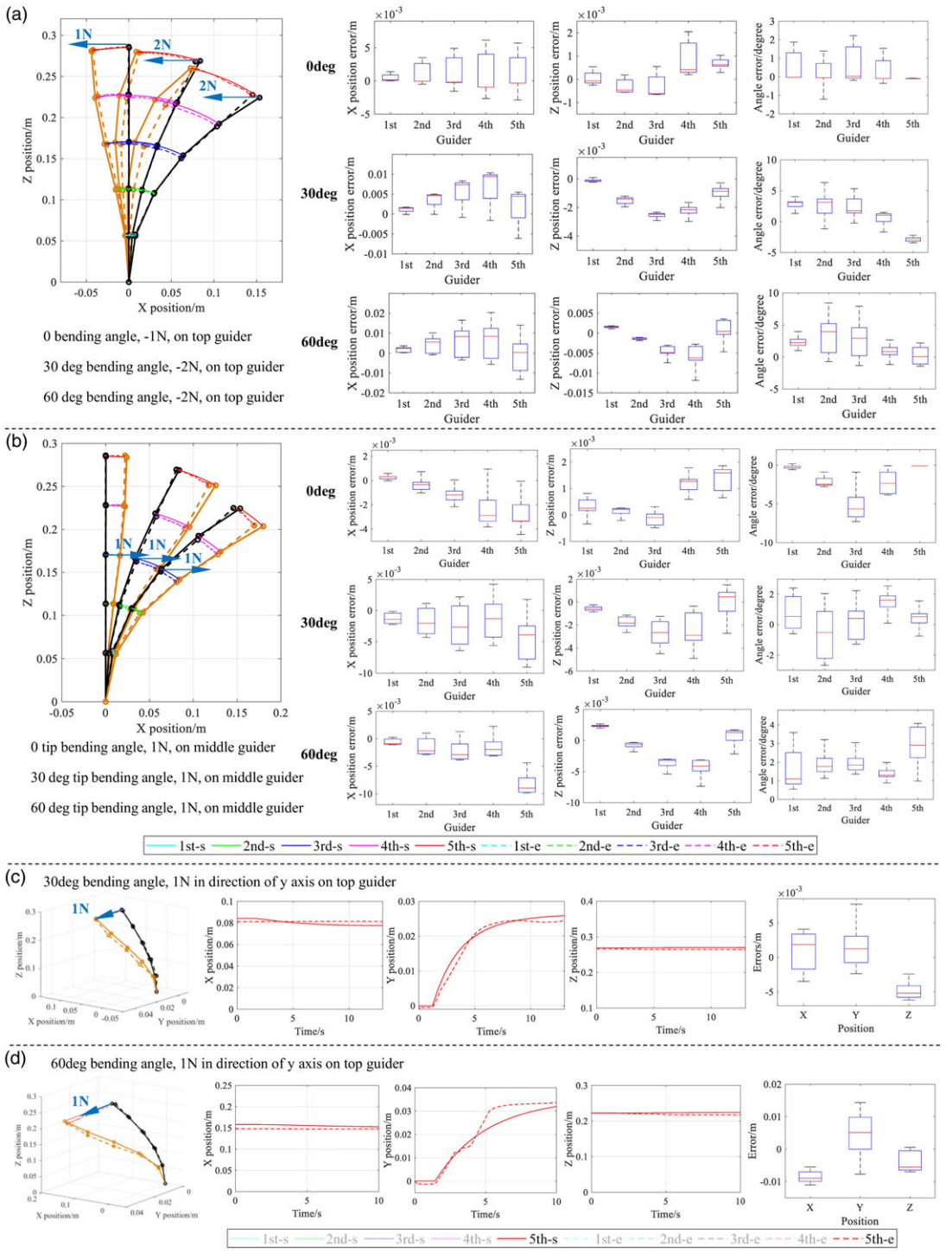

Figure 10. *Illustration of deformation under external force in different conditions: (a) and (b) show the track, position, and bending angle comparison of the whole posture for 0°, 30°, and 60° with (−1N, −2N, and −2N) on the top guider and (1N, 1N, 1N) on the middle guider, respectively; (c) shows the track and position comparison of top guider for 30° with 1N; (d) shows the track and position comparison of top guider for 60° with 1N.*

https://doi.org/10.1017/S0263574724001735 Published online by Cambridge University Press

6.4. Shape deformation under external force

SRC-Bot exhibits low stiffness and is prone to deformation when subjected to external forces. Therefore, in this section, a series of experimental validations were conducted by comparing the simulation under external forces at various postures with different bending angles.

The initial stages of the experiment focused on the in-plane deflection, with bending angles set at 0°, 30°, and 60°, and external forces of 1N or 2N applied to the top or middle guider within the xoz plane. Figure 10(a) and (b) present a comparison of the position in the xoz plane and the bending angle of each guider from the first to the fifth.

As illustrated in Figure 10(a), an external force in a negative direction along the x-axis was exerted on the top guider, resulting in bending angles of 0°, 30°, and 60°. The position errors in the x and z directions of each guider with a 0° bending angle and an external force of −1N exhibited significant fluctuation, ranging from −5.2 mm to 5.3 mm. Similarly, the errors in the bending angle of each guider spanned a considerable range, from −2° to 3°. The positional errors were more pronounced when the initial bending angle was increased to 30° and the external force was increased to −2N. In this case, the errors in the x direction and z direction were within ±9.7 mm and ±3.2 mm, respectively, while the errors in the bending angle of each guider varied between -3.0° and 7.5°.

Then the initial bending angle was set to 60°, and the external force was −2N. Similarly, the errors of position in the x and z direction were within ±2.8 mm and ±7.1 mm, respectively, and the errors of bending angle for each guider were within −2.5° to 9.1°. Conversely, the direction of external force was changed to positive in the x direction and acting on the middle guider as shown in Figure 10(b). When the bending angle initial posture was 0°, the position errors were between −5.1 mm and 2.4 mm, and the bending angle errors tended to be negative with a minimum value of −7.5°.

Subsequently, the position errors became larger within the range from −8.9 mm to 5.1 mm, and the bending angle errors floated in ±2.5° as the initial bending angle enlarged to 30°. Thereafter, the bending angle of the initial posture was set to 60°, and a 1N external force was applied on the middle guider. The results show that the position errors in both the x and z direction were between −9.8 mm and 5.0 mm, and errors of bending angle were from 0.2° to 4.6°. Upon comparing the deformation with external force in-plane, it was observed that the position and angle errors of each guider remained minimal when the posture deflected from the vertical status by 0°. However, these errors progressively increase as the initial bending angle rises to 30° and even 60°. The simulation conducted using the proposed theoretical model closely aligned with the experimental results overall. However, the simulated posture exhibited a slight over-deformation compared to the physical robot, primarily due to stiffness inconsistencies.

The model's validity was further assessed by incorporating spatial external forces in a comparative experiment, as illustrated in Figure 10(c) and (d). In Figure 10(c), a horizontal external force along the positive y-direction is applied to the top guider of the bent physical robot with an initial posture of 30°. The 3-dimensional position errors are within ±10.0 mm, and the deformed trajectory of the top guider closely matches the experimental results. Subsequently, with the initial bending angle set to 60°, the deformation comparisons demonstrate reasonable consistency, with 3-dimensional position errors ranging from −15.1 mm to 19.3 mm.

In summary, the proposed dynamics model effectively captures the deformable behavior of SRC-Bot under various actuation and external forces. However, minor discrepancies in the quantitative comparisons are observed, primarily due to differences between the actual robot's stiffness and the identified values. Furthermore, the deviations in theoretical damping ratio and friction coefficient contribute to slight errors in the response and steady-state behavior over time.

7. Conclusions and future works

This work proposes a modeling approach with variable curvature-torsion-length for a switchable rigid-continuum robot, aiming to specify the deformation response and behavior under various actuation and external forces. An equivalence and discretization method is employed in motion analysis for both

https://doi.org/10.1017/S0263574724001735 Published online by Cambridge University Press

kinematics and dynamics, dividing the robot into multiple segments with corresponding stiffness based on the number of internal guiders. The dynamics model is formulated by incorporating the influences of gravity, friction, and external forces using Newton's second law and Euler's principle while integrating an equivalent concept to determine stiffness parameters. The theoretical dynamics model is then implemented in SIMULINK to simulate the deformable response under various input forces. Equivalent stiffnesses, determined through a set of identification experiments, are employed in corresponding simulations. Finally, a series of experiments are conducted to validate the established dynamics model, focusing on the trajectory of each guider and posture deformation under actuation and external forces.

The numerical comparisons reveal that the posture deformations observed in simulated and experimental results generally exhibit consistency, albeit with slight deviations. These results clearly demonstrate that the proposed dynamics model effectively captures the deformable behavior exhibited by the physical SRC-Bot. Notably, properties such as stiffness, damping ratio, and friction coefficient require manual identification or definition due to the robot's irregular shape and assembled structure, leading to discrepancies in static posture and temporal response. Future work will focus on enhancing the model's precision and exploring its application in controller design.

Author contributions. YD and HW conceived the idea and devised the formulation. HW conducted the simulations. YD conducted the experiments. YD and HW wrote the article. SZ and ZZ reviewed the article. HW supervised the work.

Financial support. None.

Competing interests. The authors declare no competing interests exist.

Ethical approval. None.

References

[1] I. D. Walker, "Continuous backbone "continuum" robot manipulators," *Int. Scholarly Res. Not.* **2013**(1), 1–19 (2013).
[2] T. D. Nguyen and J. Burgner-Kahrs, "A Tendon-driven Continuum Robot with Extensible Sections," **In:** *IEEE/RSJ International Conference on Intelligent Robots and Systems* (2015) pp. 2130–2135.
[3] M. Wang, X. D. D.Palmer, D. A. D.Alatorre and A. Norton, "Design and Development of a Slender Dual-structure Continuum Robot for In-situ Aeroengine Repair," **In:** *IEEE/RSJ International Conference on Intelligent Robots and Systems* (2018) pp. 5648–5653.
[4] D. Alatorre, B. Nasser, A. Rabani, A. Nagy-Sochacki, X. Dong, D. Axinte and J. Kell, "Teleoperated, in situ repair of an aeroengine: Overcoming the internet latency hurdle," *IEEE Robot. Automat. Mag.* **26**(1), 10–20 (2018).
[5] J. Burgner-Kahrs, D. C. Rucker and HChoset, "Continuum robots for medical applications: A survey," *IEEE Trans. Robot.* **31**(6), 1261– (1280, 2015).
[6] H. Su, D. C. Cardona, W. Shang, A. Camilo, G. A. Cole, D. C. Rucker and G. S. Fischer, "A MRI-Guided Concentric Tube Continuum Robot with Piezoelectric Actuation: A Feasibility Study," **In:** *IEEE International Conference on Robotics and Automation* (2012), pp.1939–1945.
[7] W. McMahan, V. Chitrakaran, M. Csencsits, D. Dawson, I. D. Walker, B. A. Jones and C. D. Rahn, "Field Trials and Testing of the OctArm Continuum Manipulator," **In:** *IEEE International Conference on Robotics and Automation* (2006), pp. 2336–2341 (
[8] B. He, Z. Wang, Q. Li, H. Xie and R. Shen, "An analytic method for the kinematics and dynamics of a multiple-backbone continuum robot," *Int. J. Adv. Robot. Syst.* **10**(1), 84 (2013).
[9] S. Cobos-Guzman, D. Palmer and D. Axinte, "Kinematic model to control the end-effector of a continuum robot for multi-axis processing," *Robotica* **35**(1), 224–240 (2017).
[10] X. Zhang, Y. Liu, D. T. Branson, C. Yang, J. S. Dai and R. Kang, "Variable-gain control for continuum robots based on velocity sensitivity," *Mech. Mach. Theory* **168**, 104618 (2022).
[11] J. Yang, H. Peng, W. Zhou, J. Zhang and Z. Wu, "A modular approach for dynamic modeling of multisegment continuum robots," *Mech. Mach. Theory* **165**, 104429 (2021).
[12] A. Amouri, C. Mahfoudi and A. Zaatri, "Dynamic modeling of a spatial cable-driven continuum robot using euler-lagrange method," *Int. J. Eng. Technol. In.* **10**(1), 60 (2019).
[13] T. da Veiga, J. H. Chandler, P. Lloyd, G. Pittiglio, N. J. Wilkinson, A. K. Hoshiar and P. Valdastri, "Challenges of continuum robots in clinical context: A review," *Prog. Biomed. Eng.* **2**(3), 032003 (2020).
[14] M. T. Chikhaoui and Burgner-Kahrs J., "Control of continuum robots for medical applications: State of the art," **In:** *International Conference on New Actuators*, pp. 1–11 (2018).

https://doi.org/10.1017/S0263574724001735 Published online by Cambridge University Press

[15] S. M. Mustaza, Y. Elsayed, C. Lekakou, C. Saaj and J. Fras, "Dynamic modeling of fiber-reinforced soft manipulator: A visco-hyperelastic material-based continuum mechanics approach," *Soft Robot.* **6**(3), 305–317 (2019).
[16] M. T. Chikhaoui, K. Rabenorosoa and N. Andreff, "Kinematics and performance analysis of a novel concentric tube robotic structure with embedded soft micro-actuationm," *Mecha. Mach. Theory.* **104**, 234–254 (2016).
[17] Della Santina C., Bicchi A.and Rus D., "On an improved state parametrization for soft robots with piecewise constant curvature and its use in model based control," *IEEE Rob. Autom. Lett.* **5**(2), 1001–1008 (2020).
[18] R. J. Webster III and B. A. Jones, "Design and kinematic modeling of constant curvature continuum robots: A review," *Int. J. Robot. Res.* **29**(13), 1661–1683 (2010).
[19] J. Lai, K. Huang, B. Lu, Q. Zhao and H. K. Chu, "Verticalized-tip trajectory tracking of a 3D-printable soft continuum robot: Enabling surgical blood suction automation," *IEEE-ASME Trans. Mech.* **27**(3), 1545–1556 (2021).
[20] S. Song, Z. Li, H. Yu and H. Ren, "Shape reconstruction for wire-driven flexible robots based on Bézier curve and electromagnetic positioning," *Mechatronics.* **29**, 28–35 (2015).
[21] F. Xu, Y. Zhang, J. Sun and H. Wang, "Adaptive visual servoing shape control of a soft robot manipulator using bezier curve features," *IEEE-ASME Trans. Mech* **28**(2), 945–955 (2022).
[22] W. S. Rone and P. Ben-Tzvi, "Continuum robot dynamics utilizing the principle of virtual power," *IEEE Trans. Robot.* **30**(1), 275–287 (2013).
[23] V. Falkenhahn, T. Mahl, A. Hildebrandt, R. Neumann and O. Sawodny, "Dynamic modeling of bellows-actuated continuum robots using the Euler–Lagrange formalism," *IEEE Trans. Robot.* **31**(6), 1483–1496 (2015).
[24] M. Wang, X. Dong, W. Ba, A. Mohammad, D. Axinte and A. Norton, "Design, modelling and validation of a novel extra slender continuum robot for in-situ inspection and repair in aeroengine," *Robot. Cim-Int. Manuf.* **67**, 102054 (2021).
[25] F. Renda, M. Giorelli, M. Calisti, M. Cianchetti and C. Laschi, "Dynamic model of a multibending soft robot arm driven by cables," *IEEE Trans. Robot.* **30**(5), 1109–1122 (2014).
[26] D. C. Rucker and R. J. Webster III, "Statics and dynamics of continuum robots with general tendon routing and external loading," *IEEE Trans. Robot.* **27**(6), 1033–1044 (2011).
[27] J. Till, V. Aloi and C. Rucker, "Real-time dynamics of soft and continuum robots based on Cosserat rod models," *Int. J. Robot. Res.* **38**(6), 723–746 (2019).
[28] S. Grazioso, G. Di Gironimo and B. Siciliano, "A geometrically exact model for soft continuum robots: The finite element deformation space formulation," *Soft Robot.* **6**(6), 790–811 (2019).
[29] Z. Liu, X. Zhang, Z. Cai, H. Peng and Z. Wu, "Real-time dynamics of cable-driven continuum robots considering the cable constraint and friction effect," *IEEE Rob. Autom. Lett.* **6**(4), 6235–6624 (2021).
[30] N. Simaan, "Snake-like Units Using Flexible Backbones and Actuation Redundancy for Enhanced Miniaturization," **In:** *IEEE International Conference on Robotics and Automation*, pp. 3012–3017 (2005).
[31] M. T. Chikhaoui, K. Rabenorosoa and N. Andreff, "Kinematic Modeling of an EAP Actuated Continuum Robot for Active Micro-Endoscopy," In: *Advances in Robot Kinematics* (2014) pp. 457–465.
[32] Y. Chitalia, N. J. Deaton, S. Jeong, N. Rahman and J. P. Desai, "Towards FBG-based shape sensing for micro-scale and meso-scale continuum robots with large deflection," *IEEE Rob. Autom. Lett.* **5**(2), 1712–1719 (2020).
[33] H. Wang, Z. Zhou, X. Yang and Zhang A., "Switchable Rigid-Continuum Robot Arm: Design and Testing," **In:** *IEEE International Conference on Robotics and Automation*, pp. 5162–5169 (2022).

Appendix

A. Nomenclature

θ_{vi}	Bending angle of i^{th} guider
θ_v	Bending angle of top guider
$\omega_{\theta vi}$	Bending angular velocity of the ith guider
$\dot{\omega}_{\theta vi}$	Bending angular acceleration of the i^{th} guider
φ_{vi}	Rotation angle of the i^{th} guider
φ_v	Rotation angle of the bottom guider
$\omega_{\varphi vi}$	Rotation angular velocity of the i^{th} guider
$\dot{\omega}_{\varphi vi}$	Rotation angular acceleration of the i^{th} guider
L_{vi}	Length of the i^{th} guider
L_v	Total length of the robot
L_0	Natural length of the chamber
$a_{L_{vi}}$	Acceleration of the i^{th} guider

https://doi.org/10.1017/S0263574724001735 Published online by Cambridge University Press

C_0	Chord length with a natural arc length
L_0	Natural length of the chamber
C_{vi}	Chord length between the $(i-1)^{th}$ and i^{th} guider
$\dot{C}_{vi}$	Change rate of chord length
L_{di}	Length of driven cable
(x_{vi}, y_{vi}, z_{vi})	Coordinates of the ith guider
(x_i, y_i, z_i)	Coordinates of the top guider
P_{vi}	Relative translation of i^{th} guider
P_i	translation of top guider
$\mathcal{M}_{vi}$	Revolute motion matrix of i^{th} guider
T_{vi}	Homogeneous transformation matrix of i^{th} guider
$\mathbf{M}_{tevi}$	Total moment generated by the external force $\mathbf{F}_{evi}$
$\mathbf{M}_{tgvi}$	Total moment generated by the gravity effect $\mathbf{G}_{gvi}$
$\mathbf{M}_{tinvi}$	Total moment generated by inertia force $\mathbf{F}_{invi}$
$\mathbf{F}_{invi}$	Inertia force of each guider
$\mathbf{F}_{evi}$	External force
$\mathbf{G}_{gvi}$	Gravity effect
${}^{j}F_i$	Actuation force transmitted from the motor acting on i^{th} cable across j^{th} guider
F_i	Output force from the motor to the i^{th} cable
${}^{j}F_{ni}$	Normal force generated by the actuation force across each j^{th} guider
${}^{j}f_i$	Friction force generated by the actuation force across each j^{th} guider
τ_θ	Generalized torque in the bending direction
τ_φ	Generalized torque in the rotation direction
f_L	Generalized force in linear motion direction
$\overline{EI}$	Equivalent bending stiffness
$\overline{GA}$	Equivalent torsional stiffness
$\overline{K}$	Equivalent linear stiffness
d_θ	Damping coefficient in the bending direction
d_φ	Damping coefficient in the rotation direction
d_L	Damping coefficient in linear motion direction
$J_{\theta vi}$	Moment inertia in the bending direction
$J_{\varphi vi}$	Moment inertia in the rotation direction
H	Friction coefficient
m_i	Mass of i^{th} guider
D_c	Diameter of the circle where the cable holes are located
J_d	Jacobian matrix

Cite this article: Y. Du, S. Zhang, Z. Zhang and H. Wang (2024). "Shape deformation analysis and dynamic modeling of a switchable rigid-continuum robot", Robotica **42**, 3934–3956. https://doi.org/10.1017/S0263574724001735